Emergent phenomena at oxide interfaces studied with standing-wave photoelectron spectroscopy (F)

(iD) **Cheng-Tai Kuo, Giuseppina Conti,** (iD) **Julien E. Rault, et al.**

COLLECTIONS

Paper published as part of the special topic on Commemorating the Career of Charles S. Fadley

(F) This paper was selected as Featured

View Online   Export Citation   CrossMark

ARTICLES YOU MAY BE INTERESTED IN

Spin- and time-resolved photoelectron spectroscopy and diffraction studies using time-of-flight momentum microscopes
Journal of Vacuum Science & Technology A **40**, 020802 (2022); https://doi.org/10.1116/6.0001500

Practical guide for curve fitting in x-ray photoelectron spectroscopy
Journal of Vacuum Science & Technology A **38**, 061203 (2020); https://doi.org/10.1116/6.0000377

Practical guides for x-ray photoelectron spectroscopy: Quantitative XPS
Journal of Vacuum Science & Technology A **38**, 041201 (2020); https://doi.org/10.1116/1.5141395

Emergent phenomena at oxide interfaces studied with standing-wave photoelectron spectroscopy Ⓕ

Cheng-Tai Kuo,[1] ⒾⒹ Giuseppina Conti,[2,3] Julien E. Rault,[4] ⒾⒹ Claus M. Schneider,[3,5] ⒾⒹ Slavomír Nemšák,[2,a)] ⒾⒹ and Alexander X. Gray[6,a)] ⒾⒹ

AFFILIATIONS

[1]Stanford Synchrotron Radiation Lightsource, SLAC National Accelerator Laboratory, Menlo Park, California 94025
[2]Advanced Light Source, Lawrence Berkeley National Laboratory, Berkeley, California 94720
[3]Department of Physics, University of California, Davis, Davis, California 95616
[4]Synchrotron-SOLEIL, Saint-Aubin, BP48, F91192 Gif sur Yvette Cedex, France
[5]Peter Grünberg Institut (PGI-6), Forschungszentrum Jülich GmbH, D-52425 Jülich, Germany
[6]Department of Physics, Temple University, Philadelphia, Pennsylvania 19122

Note: This paper is a part of the Special Collection Commemorating the Career of Charles S. Fadley.
[a)]Authors to whom correspondence should be addressed: snemsak@lbl.gov and axgray@temple.edu

ABSTRACT

Emergent phenomena at complex-oxide interfaces have become a vibrant field of study in the past two decades due to the rich physics and a wide range of possibilities for creating new states of matter and novel functionalities for potential devices. The electronic-structural characterization of such phenomena presents a unique challenge due to the lack of direct yet nondestructive techniques for probing buried layers and interfaces with the required Ångstrom-level resolution, as well as element and orbital specificity. In this Review, we survey several recent studies wherein soft x-ray standing-wave photoelectron spectroscopy—a relatively newly developed technique—is used to investigate buried oxide interfaces exhibiting emergent phenomena such as metal-insulator transition, interfacial ferromagnetism, and two-dimensional electron gas. The advantages, challenges, and future applications of this methodology are also discussed.

Published under an exclusive license by the AVS. https://doi.org/10.1116/6.0001584

I. INTRODUCTION

The x-ray standing-wave (SW) technique was pioneered by Batterman in the early 1960s[1] and was used extensively over the next several decades to tackle a wide variety of surface science problems, such as solving structures of adsorbates,[2] investigating the localization of impurities,[3] and surface reconstructions.[4] All of the above-mentioned studies utilized standing-wave formation by Bragg reflection from atomic planes and were carried out in the hard x-ray regime, which is ideally suited for atomic-resolution crystallographic studies due to the characteristic subnanometer wavelengths. The basic principles and history of the standing-wave technique, including notable seminal studies, are described in detail in the book by Zegenhagen and Kazimirov[5] as well as several recent topical reviews.[6–8]

Standing-wave studies of the (buried) complex-oxide interfaces were, to a large degree, made possible by the extension of the standing-wave technique into the soft x-ray regime applied to artificial superlattices, which benefited greatly from the higher photoionization cross sections, better energy resolution, and, significantly, easier collection of electron-momentum-resolved data. Although the earliest studies by Yang *et al.*[9] and by Kim and Kortright[10] focused on magnetic interfaces, such as Fe/Cr and Co/Pd, and took advantage of the x-ray magnetic circular dichroism (XMCD) effects at the transition-metal *L* edges and/or 2*p* core-level photoemission peaks, in the 2010s, following the discoveries of emergent phenomena,[11–13] the focus shifted to strongly correlated perovskite oxides.

Over the recent decade, the research group of Charles S. Fadley, celebrated in this focus issue, has utilized soft x-ray standing-wave spectroscopy in conjunction with other experimental techniques to study a wide variety of complex-oxide interface systems exhibiting emergent electronic and magnetic phenomena.[14–22] Their experimental progress was met by the collaborators on the theory and computation

side with the development of advanced x-ray optical codes for fitting and optimization of the standing-wave data,[23,24] as well as modeling of the depth-resolved electronic structure via advanced Green's function methods, such as the one-step theory of photoemission.[25,26] In the latter part of the decade, the second generation of researchers originating from Fadley's group and its collaborators have continued this rich scientific tradition with the most recent studies of interfacial charge reconstructions,[27] structural distortions,[28] and electrochemically driven surface transformations.[29]

In this article, we overview several key studies from this period, with the specific focus on the depth-resolved investigations of the emergent interfacial phenomena in oxide systems. Among such phenomena, we focus on the interfacial metal-insulator transition (MIT) in $LaNiO_3/SrTiO_3$,[15] the occurrence of a two-dimensional ferromagnetism in $LaNiO_3/CaMnO_3$,[27] the formation of a two-dimensional electron gas (2DEG) in $GdTiO_3/SrTiO_3$,[18,19] and the built-in electrostatic potential in $LaCrO_3/SrTiO_3$ superlattices.[21] We point out the importance of x-ray optical calculations and modeling in such studies, as well as the complementary role of first-principles theory for the interpretation of the experimental data. We also stress the strong synergy between x-ray standing-wave spectroscopy and other advanced characterization techniques, such as scanning transmission electron microscopy (STEM) with electron energy loss spectroscopy (EELS), x-ray absorption spectroscopy (XAS), as well as other modalities of photoelectron spectroscopies, such as hard x-ray photoemission and soft x-ray angle-resolved photoelectron spectroscopy (ARPES).

II. BASIC PRINCIPLES AND EXPERIMENTAL CONSIDERATIONS

To illustrate the basic principles of the soft x-ray standing-wave photoemission spectroscopy, Fig. 1(a) (from Ref. 17) depicts the schematics of a typical standing-wave "rocking-curve" measurement, wherein photoemission yields from various core levels in an oxide superlattice are collected as a function of the x-ray grazing incidence angle θ. The simulated intensity of the electric field (E^2) of the standing wave inside the sample is shown in Fig. 1(b) as a function of the depth and grazing incidence angle. It can be seen that, by scanning the x-ray grazing incidence angle θ in the vicinity of the first-order Bragg condition (~12.7°), one effectively varies the phase of the standing-wave within the sample by approximately half of the period of the superlattice. Thus, for a carefully chosen experimental geometry (e.g., θ = 12.4°), the standing-wave field could be used to highlight the "bulklike" central region of the buried $La_{0.7}Sr_{0.3}MnO_3$ layers (see Line Cut 1), while at θ = 12.9°, the electric field intensity is the highest in the interfacial regions of the $La_{0.7}Sr_{0.3}MnO_3$ layer (see Line Cut 2). In a typical experiment, the grazing incidence angle is varied continuously across the Bragg condition, resulting in a "vertical scan" of the x-ray standing wave through the superlattice sample.

It is important to note that, although the x-ray field of the standing-wave penetrates deep into the sample, the actual probing depth in the soft x-ray standing-wave photoemission experiment is limited by the inelastic mean-free path (IMFP) of the emitted photoelectrons. In a typical soft x-ray kinetic-energy range between 600 and 1200 eV, such IMFPs in transition-metal oxides are on the order of 2–3 nm. Therefore, in the specific case of the $La_{0.7}Sr_{0.3}MnO_3/SrTiO_3$ superlattice shown in Fig. 1,[17] the majority of the detected photoemission signal originates from the topmost repeat (period) of the superlattice. Since this is generally the case for most of the soft x-ray standing-wave photoemission studies, including the four examples described in this Review, special considerations should often be given to the possible differences between the bulk of the superlattice and the truncated surface. For example, in a recent soft x-ray standing-wave photoemission study of the $Eu_{0.7}Sr_{0.3}MnO_3/La_{0.7}Sr_{0.3}MnO_3$ superlattice,[28] Yang et al. have demonstrated that the topmost unit cell of the $Eu_{0.7}Sr_{0.3}MnO_3$ layer exhibits a surface reconstruction (relaxation), characterized by the presence of sites with tetrahedral oxygen coordination. Thus,
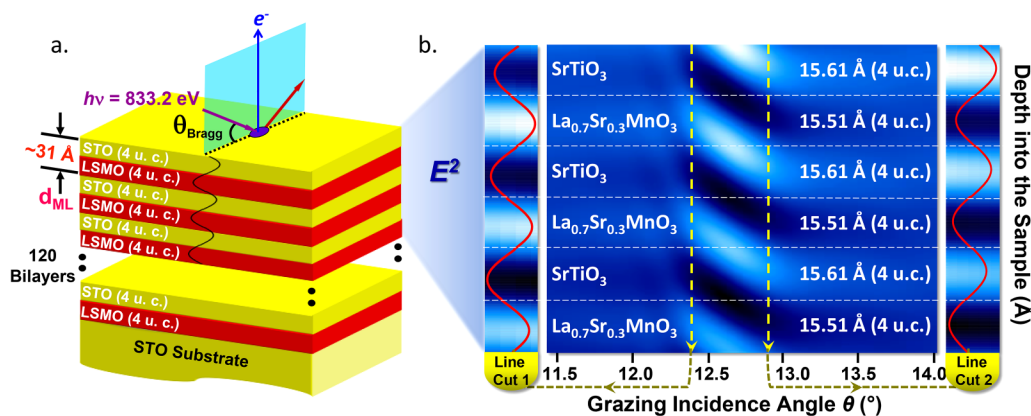
FIG. 1. (a) Schematics of the experimental geometry and the investigated multilayer structure in a typical soft x-ray standing-wave photoemission experiment. (b) Simulated intensity of the x-ray standing-wave electric field (E^2) inside the sample as a function of depth and grazing incidence angle theta. The line cuts indicate that, for incidence angles <12.4°, the standing-wave field highlights the bulk or center of the $La_{0.7}Sr_{0.3}MnO_3$ layer, but for angles >12.9°, the interface regions of the $La_{0.7}Sr_{0.3}MnO_3$ layer are emphasized. Reprinted with permission from Gray et al., Europhys. Lett. **104**, 17004 (2013). Copyright 2013, Institute of Physics.

the theoretical analysis and the x-ray optical modeling of the standing-wave data are required to account for such a surface layer with modified electronic and structural properties.

The above-mentioned sensitivity of the soft x-ray standing-wave photoemission to the several topmost layers of the superlattice could sometimes be used to an experimental advantage. For example, for oxide systems where the growth of a binary superlattice consisting of tens of periods (repeats) presents a major challenge, a better-behaved (easier to grow) epitaxial multilayer system could sometimes be used as a substrate and the standing-wave generator for the bilayer of interest. Such a strategy has been successfully utilized in multiple studies of interfaces between polycrystalline films, where Mo/Si or B$_4$C/W multilayer mirrors were utilized as the standing-wave generating substrates for various heterostructures of scientific and technological significance[6,9] and has been recently suggested for the studies of epitaxial oxide systems.[7,30]

In general, the design of an oxide superlattice that is optimized for the soft x-ray standing-wave measurement can be a challenging task and requires the combined expertise of the film grower, the spectroscopist, and the instrument scientist at the synchrotron source. For example, it is usually beneficial to tune the photon energy of the soft x rays to the core-level resonance of one of the elements in the multilayer in order to enhance the optical contrast between the alternating layers.[14,15,18] The choice of the x-ray photon energy will determine the incidence angle of the first-order Bragg condition for a superlattice of a given periodicity and, therefore, will dictate the experimental geometry for the standing-wave experiment. In a hypothetical scenario in which such an experimental geometry is not readily accessible due to the instrumental constraints (e.g., manipulator design or the orientation of the analyzer), a sample may need to be redesigned with a new periodicity that is compatible with the experimental setup. Other practical challenges, such as the mitigation of the surface charging effects, which are ubiquitous in the photoemission studies of some oxides, should be considered, specifically, when choosing the topmost "termination" layer of the superlattice.

III. INTERFACIAL METAL-INSULATOR TRANSITION IN LaNiO₃/SrTiO₃

Fundamental understanding and the control of MIT in strongly correlated material systems are of direct relevance and applicability to future device design.[31] One of the potential building blocks of such devices, lanthanum nickelate LaNiO$_3$, is such a best-known example of a complex transition-metal oxide in which electronic properties can be manipulated via thickness, strain, and heteroengineering.[32–34] In bulk form, unlike any other rare-earth nickelate compound in the RNiO$_3$ series, LaNiO$_3$ remains metallic at all temperatures.[35] However, in the form of a thin film or as a constituent layer in a superlattice, it shows insulating behavior at room temperature below a critical thickness of a few unit cells.[36,37] Numerous prior studies have addressed this phenomenon in single LaNiO$_3$ layers via a combination of advanced spectroscopic techniques and state-of-the-art theoretical calculations.[32,38,39] A seminal standing-wave photoemission study by Kaiser et al. demonstrated that, in superlattices, this phenomenon is not homogeneously distributed over the thickness of the LaNiO$_3$ layer but is more pronounced near the interfaces.[15] A follow-up momentum-resolved standing-wave ARPES study by Eiteneer et al. confirmed this observation and expanded on the details of the electronic structure with additional measurements and corroborating theoretical calculations.[19]

For these studies, high-quality epitaxial superlattice samples consisting of ten bilayers of 4 unit cell (u.c.) thick LaNiO$_3$ and 3 u.c. thick SrTiO$_3$ were grown on a (001) (LaAlO$_3$)$_{0.3}$ × (Sr$_2$AlTaO$_3$)$_{0.7}$ substrate via rf magnetron sputtering. Standard characterization techniques such as x-ray diffraction (XRD) and high-resolution STEM were used to verify the coherent epitaxy and the sharpness of the interfaces, while the results of the electronic transport measurements confirmed the metallicity of the superlattice. Standing-wave photoemission experiments were carried out at beamline 7.0.1 of the Advanced Light Source and the photon energy near the La 3$d_{5/2}$ absorption resonance (833.2 eV) in order to maximize the x-ray standing-wave node-to-antinode E-field contrast, as previously done by Gray et al. in the studies of manganite multilayers.[14,17]

For the standing-wave measurements, the core-level intensities for each constituent element in the superlattice were measured and modeled as a function of the x-ray grazing incidence angle near the first-order Bragg condition as shown in Fig. 2(a). The best fits (solid curves) to the experimental data (round symbols) obtained using an x-ray optical theoretical code[23] yielded an Ångstrom-level depth-resolved chemical profile of the sample, with some of the resultant values, such as layer thicknesses and interdiffusion lengths, shown in Fig. 2(f).

The key result of the study by Kaiser et al. comes from the standing-wave measurement and spectral decomposition of the high-resolution valence-band spectra of the superlattice. Figure 2(b) shows the said valence-band spectra measured as a function of the x-ray grazing incidence angle and depicted as a two-dimensional color intensity map. In this representation, it is immediately evident that different spectral regions of the valence-band manifold exhibit markedly different angular behavior. For example, it is clear that the two main intensity maxima observed at the binding energies of approximately 1 and 7 eV and marked with the black and white arrows, respectively, occur at two angular positions that are separated by 1.4°, which roughly corresponds to the FWHM of the Bragg feature observed in the core-level SW rocking-curve measurements. This suggests that these two spectral components originate from different depths that are separated by one half-period of the superlattice. Additionally, a significant decrease in the spectral intensity is observed for angles greater than 16°, suggesting an opening of a bandgap in one of the layers.

It has been previously pointed out by Woicik et al. that the valence-band spectrum of a multilayer sample could be described to the first order of approximation by a simple superposition of the matrix-element-weighted projected densities of states (MEW-DOS) of the constituent layers.[40] Extrapolating from this observation, the measured valence-band intensities at each value of the binding energy should then show the angular dependence that could be described by a linear combination of the characteristic core-level rocking curves from the unique elements comprising the constituent layers. Thus, layer-specific valence-band spectra (MEW-DOS)
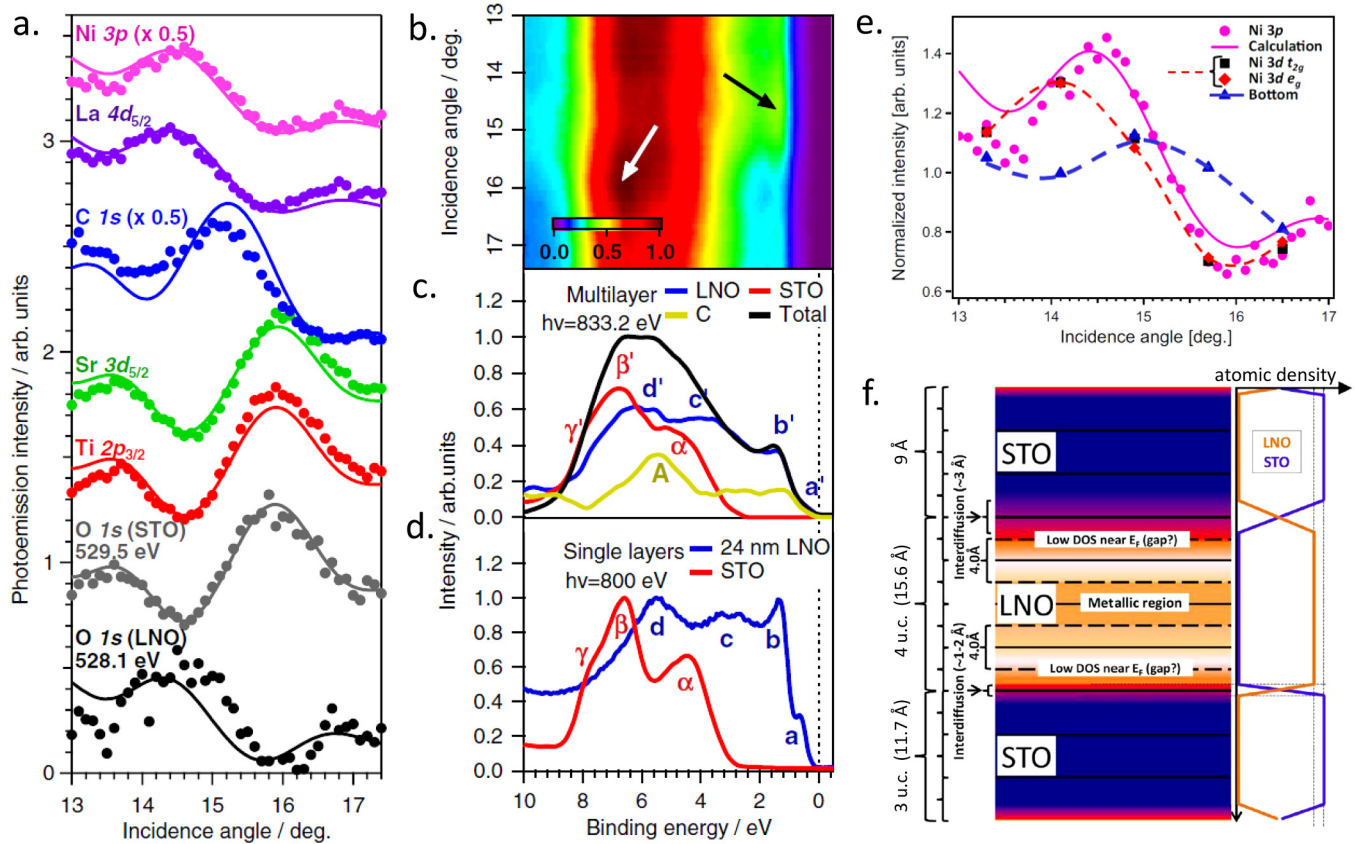
FIG. 2. (a) Experimental standing-wave rocking curves (round markers) for all relevant core levels with best theoretical fits (solid curves). (b) Intensity map of the valence band region for different incidence angles with the color scale corresponding to the photoemission yield. Two characteristic maxima split by 1.4° are marked by black and white arrows. (c) Total valence-band spectrum (black curve) of the superlattice with deconvoluted spectral components showing the characteristic angular behavior of $LaNiO_3$ (curve with Roman letter labels), $SrTiO_3$ (curve with Greek letter labels), and C-containing surface adsorbate (curve labeled A). (d) Valence-band spectra of a $SrTiO_3$ single crystal (red curve) and a bulk 24 nm-thick $LaNiO_3$ film (blue curve). Characteristic features are labeled by lowercase Latin letters for $LaNiO_3$ and Greek letters for $SrTiO_3$. (e) Integrated intensities of the Ni $3d$ t_{2g}, e_g, and the band bottom, compared to the Ni $3p$ core-level rocking curve (experiment and simulation). (f) Schematic depth profile of the first few layers of the sample, as derived from the analysis of the core-level and the valence-band rocking curves. Reprinted with permission from Kaiser *et al.*, Phys. Rev. Lett. **107**, 116402 (2011). Copyright 2011, American Physical Society; and Eiteneer *et al.*, J. Electron Spectrosc. Relat. Phenom. **211**, 70 (2016). Copyright 2016, Elsevier.

could be deconvoluted from the valence-band spectrum of the superlattice sample by using the core-level SW rocking curves for Ti $2p$ (representing $SrTiO_3$), La $4d$ (representing $LaNiO_3$), and C $1s$ (representing carbon-containing surface adsorbates) peaks.

The resultant layer-specific valence-band spectra for the $LaNiO_3$ and $SrTiO_3$ layers are shown in Fig. 2(c) and compared to the corresponding valence-band spectra obtained separately from the single bulklike films of $LaNiO_3$ and $SrTiO_3$ [Fig. 2(d)]. While the $SrTiO_3$ spectra exhibit good agreement, a significant suppression of the near-Fermi-level Ni $3d$ e_g and t_{2g} states [labeled a′ and b′] is observed for the $LaNiO_3$ layer in the superlattice sample, as compared to the bulklike film. A further quantitative investigation of the angular behavior of the near-Fermi-level region of the spectrum and its comparison to the La $4d$ (not shown here) and Ni $3p$ rocking curves [see Fig. 2(e)] reveal that the spectral weights of the Ni $3d$ e_g and t_{2g} states are preferentially suppressed within an

approximately one-unit-cell thick region of the $LaNiO_3$ film near the interface with $SrTiO_3$. A schematic diagram of the calculated interface profile is shown in Fig. 2(f). In summary, the study by Kaiser *et al.*[15] demonstrated a straightforward methodology for deriving layer-resolved valence-band spectral functions in oxide superlattices, which has been since successfully applied to several other technologically relevant material systems.[21] Furthermore, together with a later work by Eiteneer *et al.*,[19] it has furthered our understanding of the interfacial MIT physics in Mott oxides.

IV. ORIGINS OF INTERFACIAL FERROMAGNETISM IN $LaNiO_3$/$CaMnO_3$

From the early days of standing-wave photoelectron spectroscopy, it has been suggested that the standing-wave excitation could be used in conjunction with techniques such as XMCD and

STEM-EELS for the depth-resolved profiling of the interfaces between magnetic materials.[41] Consequently, over the past 20 years, several such studies have been carried out on the heterostructures of key importance in the fields of spintronics and magnetic data storage. Examples of the investigated material systems include Fe/Cr,[9] Fe/MgO,[42] and CoFeB/CoFe (Ref. 43) interfaces wherein the depth-dependence of electronic, chemical, and magnetic profiles have both scientific and technological significance.

With the advent of atomic-level oxide heteroengineering, standing-wave photoemission emerged as an ideal tool for studying new magnetic ground states at interfaces between strongly correlated oxides and the underlying electronic phenomena that are responsible for stabilizing these states. Due to its Ångstrom-level depth resolution, element and orbital specificity, and nondestructive nature, this technique is a formidable competitor of STEM-EELS and, when used in tandem with advanced microscopic techniques,[17,28] provides a comprehensive picture of the structural and electronic interactions at the interface.

Most recently, Chandrasena et al.[27] utilized soft x-ray standing-wave photoelectron spectroscopy in conjunction with STEM-EELS to demonstrate a depth-dependent charge reconstruction that leads to the emergence of interfacial ferromagnetism at the interface between paramagnetic $LaNiO_3$ and antiferromagnetic $CaMnO_3$ [Fig. 3(a)]. The stabilization of a long-range ferromagnetic order at this interface system has been discovered nearly a decade ago[44] and was consequently attributed to two distinct mechanisms: a Mn^{4+}-Mn^{3+} double exchange interaction in the interfacial

$CaMnO_3$ layer and a Ni^{2+}-O-Mn^{4+} superexchange interaction at the interface between $LaNiO_3$ and $CaMnO_3$.[45,46] These studies also revealed the presence of the necessary off-stoichiometric cations (Ni^{2+} and Mn^{3+}) in the $LaNiO_3/CaMnO_3$ heterostructures using depth-averaging techniques such as XAS and XMCD. However, until recently, no direct measurement showed unambiguously that they were localized at the interface [as shown schematically in Fig. 3(b)], where the emergent magnetic state was observed via polarized neutron reflectivity.[44]

In order to address the question of the underlying electronic origin of interfacial ferromagnetism in this material system, a high-quality epitaxial [4-u.c. $LaNiO_3$/4-u.c. $CaMnO_3$] × 15 superlattice was synthesized on top of a single-crystalline $LaAlO_3$ (001) substrate using pulsed laser deposition. Coherent epitaxy, nominal thickness, and interface quality were verified using a combination of STEM, XRD, and soft x-ray reflectivity. Bulk magnetization measurements were used to verify the presence of the ferromagnetic state, and depth-averaged XAS spectroscopy was used to confirm the presence of the mixed valence states for both Mn (4+ and 3+) and Ni (3+ and 2+). After these preliminary characterization measurements, standing-wave photoelectron spectroscopy measurements were carried out at the high-resolution ADRESS beamline of the Swiss Light Source at the photon energy near the La $3d_{5/2}$ absorption resonance, as described in Sec. III.

Core-level photoemission intensities from every constituent element in the superlattice were recorded as a function of the grazing incidence angle near the first-order Bragg condition (~14°)
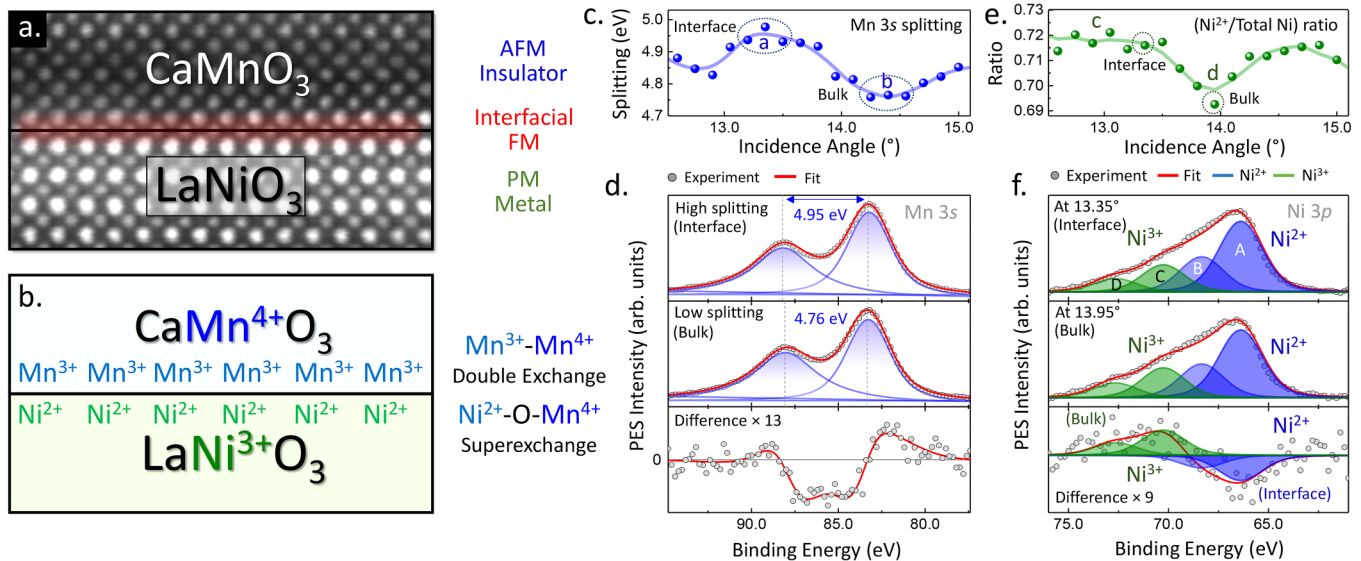
FIG. 3. (a) High-resolution STEM-HAADF cross-sectional image of the coherent epitaxial $LaNiO_3/CaMnO_3$ interface. (b) Schematic diagram of the proposed (and observed) interfacial charge reconstruction leading to the emergence of the electronic environment that is favorable for the stabilization of interfacial ferromagnetism. (c) Depth-dependent evolution of the Mn 3s multiplet splitting as a function of the x-ray grazing incidence angle. (d) Mn 3s spectra recorded in the interface-sensitive and bulklike-sensitive experimental geometries, showing an increase of the splitting, which is a spectroscopic signature of the reduced formal valency of Mn cations. (e) Plot of the relative Ni^{2+} peak(s) intensity as a function of x-ray grazing incidence angle, with the interfacelike and bulklike Ni 3p peaks shown in (f). Reprinted with permission from Chandrasena et al., Phys. Rev. B 98, 155103 (2018). Copyright 2018, American Physical Society.

and self-consistently fitted using an x-ray optical theoretical code,[23] yielding a detailed chemical profile of the sample, including thicknesses of all layers, interfacial interdiffusion lengths, as well as the angle-dependent profile of the standing-wave E-field intensity within the superlattice (see Figs. 2 and 3 in Ref. 27). Depth-resolved valence-state profiles of the Mn and Ni cations near the interface were extracted from the high-resolution spectra of the Mn 3s and Ni 3p peaks that were recorded as a function of the standing-wave position within the sample [Figs. 3(c)–3(f)]. Specifically, the depth-dependent evolution of the Mn 3s multiplet splitting [Fig. 3(c)] was utilized to determine the change in the Mn valence state[47] between the bulklike and interfacelike regions of the $CaMnO_3$ layer [Fig. 3(d)]. Conversely, the relative peak intensities of the 3+ and 2+ components of the Ni 3p core level[48] were used to track the depth-dependent evolution of the formal valency of the Ni cations in the $LaNiO_3$ layer [Figs. 3(e) and 3(f)].

The background-subtracted and fitted data shown in Figs. 3(d) and 3(f) revealed a depth-dependent charge redistribution within the $LaNiO_3$/$CaMnO_3$ heterostructure, with an increased concentration of the off-stoichiometric B-site cations (Mn^{3+} and Ni^{2+}) near the interfaces and a higher abundance of "formal valence" cations (Mn^{4+} and Ni^{3+}) in the bulklike regions of the respective layers, as shown schematically in Fig. 3(b). On the $CaMnO_3$ side of the interface, such charge reconstruction has been predicted to originate due to the leakage of itinerant 3d e_g electrons from the adjacent Ni sites in $LaNiO_3$.[44,49] Conversely, the presence of the Ni^{2+} cations on the $LaNiO_3$ side of the interface is consistent with the emergence of oxygen vacancies driven by the interfacial polar

compensation mechanism.[50] This results in an electronic environment favorable for the stabilization of interfacial ferromagnetism within a narrow (one unit cell) region at the interface and mediated by the Mn^{4+}-Mn^{3+} double exchange and/or Ni^{2+}-O-Mn^{4+} superexchange interactions. The competition between these two distinct mechanisms can be influenced by varying the thickness of $LaNiO_3$ that undergoes a metal-insulator transition in the ultrathin (few-unit-cell) limit.[45,46]

In summary, the study by Chandrasena et al.[27] established a powerful recipe for probing unit-cell-resolved changes in the interfacial valence states, resulting in the stabilization of long-range ferromagnetic order at oxide interfaces. Future works will likely extend this methodology to the polarization- and momentum-dependent studies of such material systems, thus enabling rational strategies for designing functional Mott oxide heterostructures where magnetic states could be controlled via thickness, strain, ionic defects, and external stimuli.

V. CHARACTER OF 2DEG AT THE GdTiO₃/SrTiO₃ INTERFACE

One of the biggest strengths of standing-wave photoelectron spectroscopy is its ability to specifically probe electronic properties of buried interfaces, whether they are solid/solid or, with the help of special instrumentation, solid/liquid and solid/gas.[51,52] There has been a high interest in multilayer structures involving metal oxides due to the novel electronic states that can develop at the interfaces between the different constituents, which are often very different
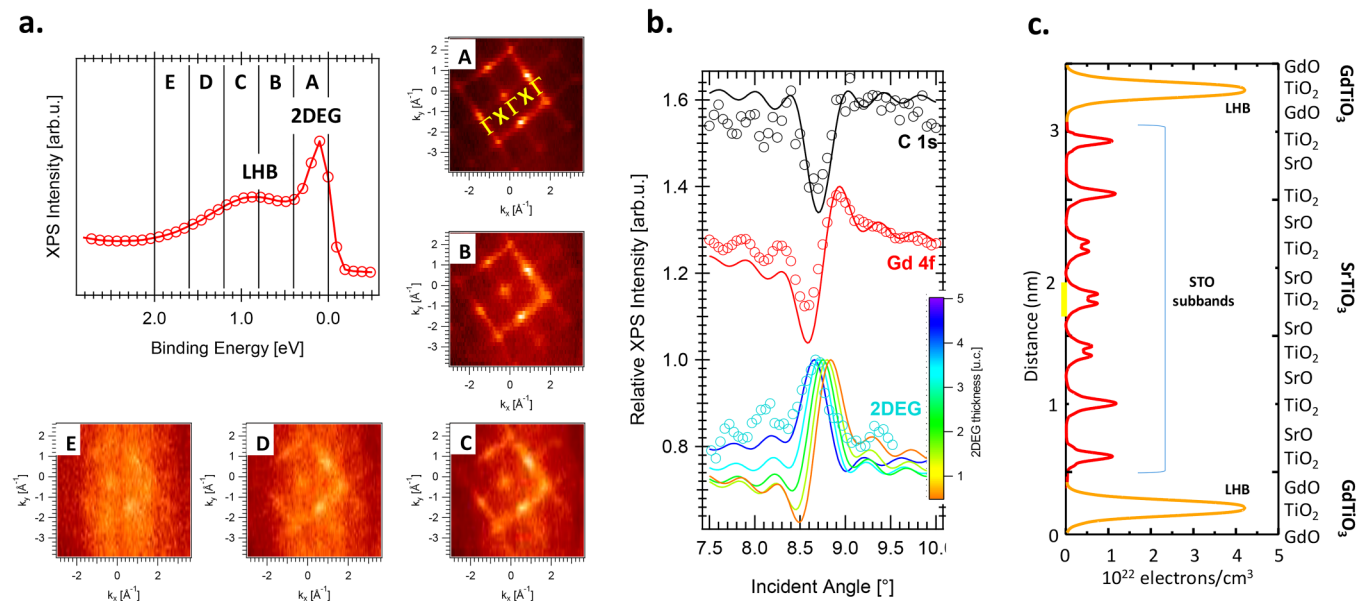
FIG. 4. (a) Angle-integrated (top left) and angle-resolved x-ray photoelectron spectroscopy data of GdTiO₃/SrTiO₃ superlattice valence band measured at a resonant excitation energy of 465.2 eV. (b) Experimental (open circles) and simulated (solid lines) rocking curves for contaminant species (C 1s), Gd 4f, and valence band peak identified as 2DEG. A 2DEG plot shows calculated rocking curves for different thicknesses of 2DEG ranging from 1 to 5 unit cells. (c) Depth-resolved sheet electron density as calculated by first-principles calculations, confirming the presence of 2DEG in the entire thickness of SrTiO₃ parts of the superlattice. Reprinted with permission from Nemšák et al., Phys. Rev. B **93**, 245103 (2016). Copyright 2016, American Physical Society.

from those states in the native bulk materials. A classic example of this phenomenon is the 2DEG at the $SrTiO_3/LaAlO_3$ interface,[53] which was discovered to be superconducting,[54] and also exhibits magnetic properties,[55] in spite of both constituents being nonmagnetic insulators. There are numerous studies that explore this system using ultraviolet and soft x-ray angle-resolved photoelectron spectroscopy as a prime tool to investigate the electronic structure of the solid materials,[56] including a standing-wave photoelectron spectroscopy study that explores the role of oxygen vacancies.[22]

Other systems exhibiting an interfacial 2DEG were discovered soon after. The $GdTiO_3/SrTiO_3$ heterostructure, for example, was studied extensively by Stemmer and collaborators, and its 2DEG exhibits extremely high carrier densities and ferromagnetic effects, with both electrostatic and doping modulation being observed to change the carrier properties.[57,58] In contrast to the case of $SrTiO_3/LaAlO_3$, the explanation for the emergence of 2DEG in $GdTiO_3/SrTiO_3$ can be found in a simple charge transfer picture.[59] Specifically, the GdO and TiO_2 planes in $GdTiO_3$ carry +1 and −1 formal ionic charges, respectively. Each GdO layer in $GdTiO_3$ can be considered to donate one-half of an electron to the TiO_2 planes above and below it, including the interfacial TiO_2 plane, which is shared with $SrTiO_3$ and in which the half-electron forms a mobile 2DEG state. Experimentally, angle-resolved photoemission provided a detailed picture of the nature of the 2DEG (including exploration of the critical thickness of $SrTiO_3$),[60] but it was an experiment with standing-wave excitation that revealed the thickness and location of 2DEG states relative to the interface.[18]

In the study by Nemšák et al., a superlattice of [6 u.c. $SrTiO_3$/ 3 u.c. $GdTiO_3$]×20 was prepared by molecular beam epitaxy and electronic transport measurements confirmed the presence of the interfacial 2DEG. The spectral and momentum signature of the 2DEG in $GdTiO_3/SrTiO_3$ is shown in Fig. 4(a). Two distinct states are resolved in the proximity of the Fermi edge. A sharp state right at the Fermi energy is identified as 2DEG, while a deeper broader peak is assigned to the lower Hubbard band (LHB) of the Mott-insulator $GdTiO_3$. The 0–2 eV binding energy range is separated into five regions, labeled A–E, and the momentum-resolved dispersive features for each of the energy regions are shown. The 2DEG dispersion follows the symmetry of the crystal, with the electron density pockets connecting Γ points of neighboring Brillouin zones. Interestingly, the deeper-located bands corresponding to the LHB show similar momentum dispersion, suggesting a somewhat similar character of these two states.

The exact depth location of the 2DEG is then studied by standing-wave photoemission. Several new approaches were used in this study, with one of them being the use of excitation energies just below and above a strong absorption edge (Gd M_5 edge in this case). Such choice of energies yields two effects—enhancement of the standing-wave modulation due to increased contrast (this was successfully demonstrated in the $La_{0.7}Sr_{0.3}MnO_3/SrTiO_3$ study by Gray et al. earlier[14]) and the inversion of the standing-wave phase, practically shifting nodes and antinodes of the standing wave by almost half a period within the superlattice. Figure 4(b) shows experimental and calculated rocking curves for the excitation energy just below the M_5 edge of Gd (1181 eV). Surface contaminants (represented by C 1s), Gd 4f, and a spectral feature [state A, Fig. 4(a)] corresponding to the 2DEG are shown. The agreement

between calculated and experimental curves for C 1s and Gd 4f confirms that the theoretical model used to simulate standing-wave data agrees very well with the experimental results, giving credibility to further analysis of the 2DEG location. The simulation of the 2DEG position revealed that it is not exclusively contained at the $GdTiO_3/SrTiO_3$ interface but expands throughout the entire thickness of the $SrTiO_3$ layers. Similar modulations (rocking curves) for the LHB states at 0.5–2 eV binding energy (not shown) and Gd 4f then suggest that LHB is located in $GdTiO_3$. These results are corroborated by first-principle calculations [shown in Fig. 4(c)], confirming that states related to the LHB are present exclusively in $GdTiO_3$ and the 2DEG occupies $SrTiO_3$ in its entire thickness.

In summary, the study by Nemšák et al.[18] provided invaluable information on the character of 2DEG, not only from the perspective of the electrons' energy and momentum but also from the physical location of these electrons in the superlattice. The enhancement of the standing wave measurements by using excitation energies below and above the absorption edge provides another way of tailoring a depth profile of the exciting x rays, and it has been since used in other studies.[21] Finally, the combination of soft and hard x-ray spectroscopy together with first-principle calculations demonstrated the synergy of such instrumentally complex studies, which are able to answer fundamental and very complicated questions on the character of the emergent electronic states at buried interfaces.

VI. DIRECT MEASUREMENT OF THE BUILT-IN ELECTROSTATIC POTENTIAL IN LaCrO₃/SrTiO₃ SUPERLATTICES

Epitaxial interfaces and superlattices of polar and nonpolar perovskite oxides have generated a considerable interest because they possess desirable properties for functional devices. For instance, Comes et al. demonstrated the existence of induced polarization fields throughout the $SrTiO_3$ layers of an $LaCrO_3/SrTiO_3$ superlattice by controlling the interfaces between polar $LaCrO_3$ and nonpolar $SrTiO_3$.[61] The induced polarization leads to built-in potential gradients within the $SrTiO_3$ and $LaCrO_3$ layers of the superlattice. Using standing-wave photoelectron spectroscopy, Lin et al explored the role of the two distinct and controllably charged interface structures $[(LaO)^+/(TiO_2)^0$ and $(SrO)^0/(CrO_2)^-]$ due to a polar discontinuity along the [001] direction and demonstrated that standing-wave photoelectron spectroscopy uniquely determines the built-in potential, along with the depth-dependent composition, and the electronic structure.[21]

The studied superlattice consisted of [5 u.c. $LaCrO_3$/10 u.c. $SrTiO_3$]×10 and was prepared by oxide molecular beam epitaxy. Figures 5(a) and 5(b) show the experimental (open circles) and simulated (solid lines) rocking curves of the representative elemental states at photon energies of 829.7 and 831.5 eV, respectively. The high quality of the superlattice is confirmed by the core-level rocking curves, which exhibit almost identical intensity profiles for the atomic species that reside in the same layer (for example, La 4d and Cr 3p, or Sr 3d and Ti 2p). On the other hand, the rocking curves corresponding to different layers, such as La 4d and Sr 3d, are out of phase with respect to each other. From the theoretical simulations of the standing wave data, it can be concluded that the
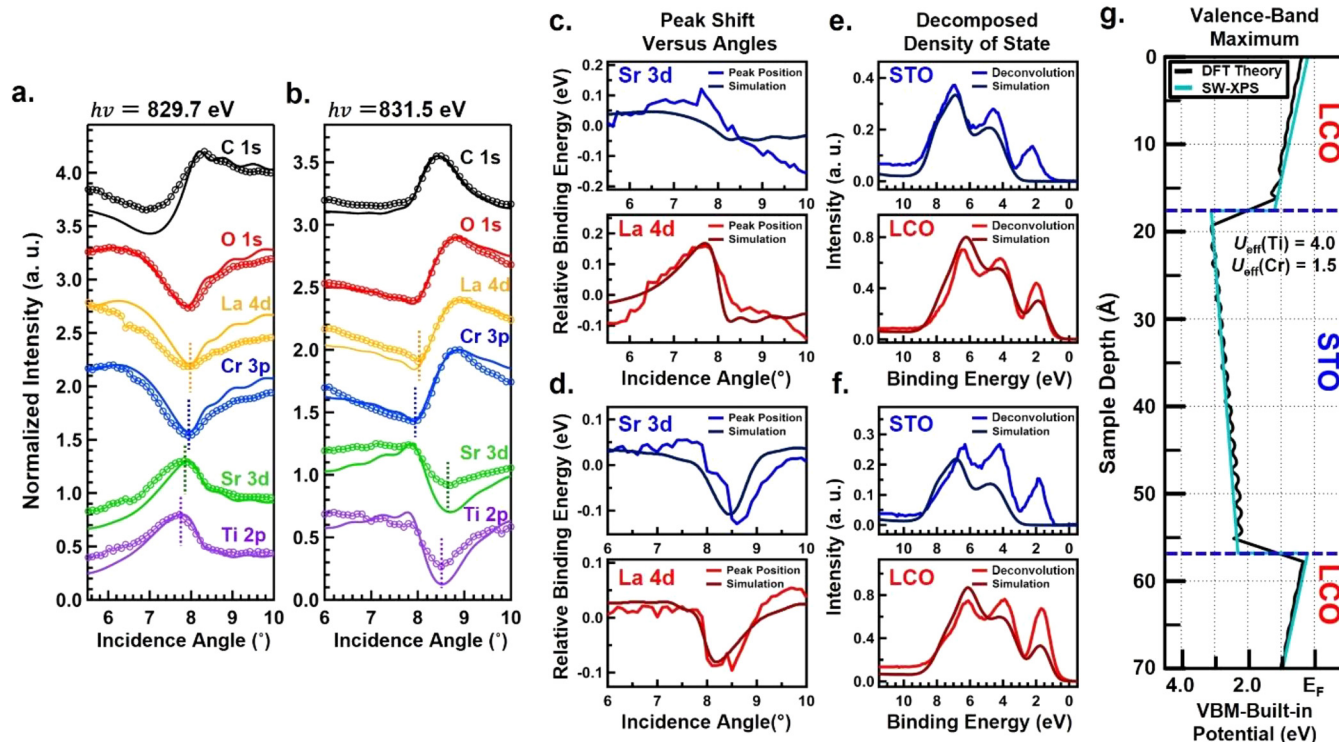
FIG. 5. Experimental (open circles) and simulated (solid) rocking curves of representative elemental states at the photon energies of (a) 829.7 and (b) 831.5 eV. The dashed vertical lines indicate the phase difference of the rocking curves. Experimental and simulated relative peak shifts for Sr 3d and La 4d core levels vs the incidence angle at the photon energies of (c) 829.7 and (d) 831.5 eV. Experimental valence-band decompositions, showing the contributions from the SrTiO₃ and LaCrO₃ layers, and corresponding simulations using XPS reference spectra from bulk SrTiO₃ and thick-film LaCrO₃, at the photon energies of (e) 829.7 and (f) 831.5 eV. (g) SW-XPS-derived (light curves) and DFT-calculated (PBEsol) depth-resolved valence-band maxima (black curves) for the top three layers of the LaCrO₃/SrTiO₃ superlattice. Reprinted with permission from Lin *et al.*, Phys. Rev. B **98**, 165124 (2018). Copyright 2018, American Physical Society.

interfaces have a roughness of ∼2–3 Å and consist of alternating positively and negatively charged structures, specifically: $(LaO)^+$/$(TiO_2)^0$ with a positive charge at the LaCrO₃(top)/SrTiO₃(bottom) interface, and $(SrO)^0$/$(CrO_2)^-$ with a negative charge at the SrTiO₃(top)/LaCrO₃(bottom) interface. These results are also consistent with the STEM-EELS studies reported in a previous work by Comes *et al.*[62] The valence-band spectrum of the superlattice sample is the sum of the MEW-DOS for all constituent layers with appropriate attenuation factors due to the electron scattering in the sample. Therefore, standing-wave modulations in the valence band exhibit a very complex behavior based on the character (and physical depth location) of the individual states. By using the core-level rocking curves as base vectors for projections of the valence-band standing-wave data, one can distinguish the valence band contributions from the LaCrO₃ or SrTiO₃ components of the superlattice, as was demonstrated earlier in the case of LaNiO₃/SrTiO₃.

For determining the built-in potential depth profile in the superlattice, the analyzes procedures involve an investigation of the apparent core-level binding energy shifts, as the standing wave is scanned through the superlattice. Figures 5(c) and 5(d) show the experimental and simulated peak shifts for the Sr 3d and La 4d

core levels versus the incidence angle at photon energies of 829.7 and 831.5 eV. The experimental Sr 3d and La 4d peak positions change in binding energy on the order of 0.1–0.2 eV around the Bragg angle. Moreover, the form of these rocking curves is quite different for the two x-ray energies due to the difference in the standing-wave phases. In the simulated peak shifts, the depth-integrated Sr 3d and La 4d spectra were calculated over the entire range of the angular scans and their angular dependences are labeled as "Simulation" in Figs. 5(c) and 5(d). The simulation assumed that the core-level binding energy follows only the built-in potential (hence, there are no chemical shifts involved) at each depth, and this potential could be described as a linear variation within each layer. The solution of the potential gradients was determined by least-square fitting. The procedure yields an excellent agreement between experiment and theory, with the exception of Sr 3d measured at the excitation energy of 829.7 eV and showing less variation in the theory. The potential gradients, labeled as "SW-XPS" (light curves in LaCrO₃ or SrTiO₃ layers), are shown in Fig. 5(g).

The energy steps or valence-band offsets at each interface are also shown in Fig. 5(g) (dashed lines in sample depths of ∼18 and

57 Å), and they are further expanded by the analysis of the valence-band maxima. The deconvoluted experimental spectra of the $SrTiO_3$ layer and $LaCrO_3$ layers are reported in Figs. 5(e) and 5(f). In these two panels, the curves denoted "Simulation" are based on summing the depth-attenuated bulklike XPS reference spectra over the entire depth of the sample shifted by the corresponding total potential [Fig. 5(g)]. The total potential $E_b^0(z_i)$ includes the potential gradients within constituent layers and steps at the polar interfaces. By combining the derivation of the slopes of the electrostatic potential within each layer and the magnitudes of the valence band offsets, we finally determine the absolute potential value with respect to the valence-band maxima, annotated as the SW-XPS-derived profile in Fig. 5(g). The results of the analysis yield a clear agreement between the qualitative expectation of the charged interface configuration and the signs of the potential gradients: higher (lower) binding energy for valence electrons at the positively (negatively) charged interfaces. The experimental results are corroborated by using density functional theory (DFT) simulations with the PBEsol density functional,[63] as implemented in the VASP code[64] with an adjustable U_{eff} parameter for d-d correlation in both layers, and these results [black curves in Fig. 5(g)] agree remarkably with the experimental results for the slopes and the offsets at the interfaces.

In summary, the study by Lin et al.[21] demonstrated the use of soft x-ray SW-XPS to extract the depth-resolved atomic and electronic structures and the built-in potential in the $LaCrO_3/SrTiO_3$ superlattice. Furthermore, the analysis of apparent binding energy shifts of the core levels and the deconvoluted valence-band spectra, as compared to theoretical simulations, has permitted the determination of the built-in potential variation with depth in great detail, including the band offsets at the polar interfaces. The experimental results are in excellent agreement with DFT, demonstrating the power and great synergy of using this experimental determination in tandem with first-principles calculations.

VII. SUMMARY AND FUTURE OUTLOOK

In this Review, we have highlighted and summarized several recent studies where soft x-ray standing-wave photoemission spectroscopy, as pioneered by Charles S. Fadley and collaborators, was utilized for the depth-resolved investigations of the emergent phenomena at the interfaces between strongly correlated perovskite oxides. Specifically, we discussed the unique advantages of the valence-band SW-XPS and SW-ARPES for the studies of interfacial metal-insulator transitions, the electronic origins of interfacial ferromagnetism, two-dimensional electron gas, and built-in potential gradients in oxide superlattices. Strong synergy with complementary spectroscopic and microscopic techniques was emphasized, as well as the key roles of x-ray optical modeling and first-principles theoretical methods, such as DFT and the one-step theory of photoemission. We believe that the future will hold many more exciting developments in the field of standing-wave photoemission, with an ever-widening variety of materials and interfaces that challenge us to understand and control the most fundamental physical processes, and at the same time, may point to potential solutions to some of our most formidable technological and societal problems.

One of the areas that carry a great promise for the future developments of standing-wave photoemission is spatially (in-plane) resolved photoemission. A full field or scanning microscopy, such as photoelectron emission microscopy or microfocused ARPES, can provide unprecedented three-dimensional pictures of the surfaces and buried interfaces with elemental and chemical sensitivity.[65,66] Inhomogeneous samples, such as exfoliated 2D materials, catalysts, nanocrystals, or patterned samples could then be studied with a high depth selectivity of the standing-wave photoemission. Another powerful combination of techniques that can be, for example, used to effectively probe interface magnetism, is a combination of standing-wave excitation with x-ray dichroism (both circular and linear). Current instrumentation developments of highly efficient spin detectors bring another possibility of combining standing-wave excitation with spin resolution.[67] In combination with micro- and nano-ARPES and/or momentum microscopy,[68,69] a standing-wave spin-resolved experiment would present a first of a kind truly complete electronic picture of a buried interface in terms of all three quantities of interest: energy, momentum, and spin.

Adding to the array of new instruments at our disposal are the x-ray free-electron lasers (FEL), providing x-ray pulses that are Fourier-transform limited in the femtosecond regime. In particular, the new high-repetition rate FELs, such as LCLS-II and XFEL, will permit us to deal more effectively with sample radiation damage and to control space-charge effects in photoemission, leading to the addition of time resolution to standing-wave spectroscopy and thus further expanding the range of questions accessible to this powerful experimental technique.

DATA AVAILABILITY

Data sharing is not applicable to this article as no new data were created or analyzed in this study.

REFERENCES

[1] B. W. Batterman, Phys. Rev. **133**, A759 (1964).

[2] B. N. Dev, G. Materlik, R. L. Johnson, W. Kranz, and P. Funke, Surf. Sci. **178**, 1 (1986).

[3] S. K. Andersen, J. A. Golovchenko, and G. Mair, Phys. Rev. Lett. **37**, 1141 (1976).

[4] J. C. Woicik, T. Kendelewicz, K. E. Miyano, P. L. Cowan, C. E. Bouldin, B. A. Karlin, P. Pianetta, and W. E. Spicer, Phys. Rev. Lett. **68**, 341 (1992).

[5] J. Zegenhagen and A. Kazimirov, *The X-Ray Standing Wave Technique Principles and Applications* (World Scientific, Singapore, 2013).

[6] S.-H. Yang, B. C. Sell, and C. S. Fadley, J. Appl. Phys. **103**, 07C519 (2008).

[7] A. X. Gray, J. Electron Spectrosc. Relat. Phenom. **195**, 399 (2014).

[8] A. X. Gray, S. Nemšák, and C. S. Fadley, Synchrotron Radiat. News **31**, 42 (2018).

[9] S.-H. Yang *et al.*, J. Phys.: Condens. Matter **14**, L407 (2002).

[10] S.-K. Kim and J. B. Kortright, Phys. Rev. Lett. **86**, 1347 (2001).

[11] K. S. Takahashi, M. Kawasaki, and Y. Tokura, Appl. Phys. Lett. **79**, 1324 (2001).

[12] A. Ohtomo, D. A. Muller, J. L. Grazul, and H. Y. Hwang, Nature **419**, 378 (2002).

[13] A. Gozar, G. Logvenov, L. Fitting Kourkoutis, A. T. Bollinger, L. A. Giannuzzi, D. A. Muller, and I. Bozovic, Nature **455**, 782 (2008).

[14] A. X. Gray *et al.*, Phys. Rev. B **82**, 205116 (2010).

[15] A. M. Kaiser *et al.*, Phys. Rev. Lett. **107**, 116402 (2011).

[16] G. Conti *et al.*, J. Appl. Phys. **113**, 143704 (2013).

[17] A. X. Gray *et al.*, Europhys. Lett. **104**, 17004 (2013).

[18] S. Nemšák *et al.*, Phys. Rev. B **93**, 245103 (2016).

[19] D. Eiteneer *et al.*, J. Electron Spectrosc. Relat. Phenom. **211**, 70 (2016).

[20] B. A. Gray *et al.*, Sci. Rep. **6**, 33184 (2016).

[21] S.-C. Lin *et al.*, Phys. Rev. B **98**, 165124 (2018).

[22] S.-C. Lin *et al.*, Phys. Rev. Mater. **4**, 115002 (2020).

[23] S.-H. Yang, A. X. Gray, A. M. Kaiser, B. S. Mun, B. C. Sell, J. B. Kortright, and C. S. Fadley, J. Appl. Phys. **113**, 073513 (2013).

[24] O. Karslıoğlu, M. Gehlmann, J. Müller, S. Nemšák, J. A. Sethian, A. Kaduwela, H. Bluhm, and C. S. Fadley, J. Electron Spectrosc. Relat. Phenom. **230**, 10 (2019).

[25] H. Ebert, D. Ködderitzsch, and J. Minár, Rep. Prog. Phys. **74**, 096501 (2011).

[26] J. Braun, J. Minár, and H. Ebert, Phys. Rep. **740**, 1 (2018).

[27] R. U. Chandrasena *et al.*, Phys. Rev. B **98**, 155103 (2018).

[28] W. Yang *et al.*, Phys. Rev. B **100**, 125119 (2019).

[29] C. Baeumer *et al.*, Nat. Mater. **20**, 674 (2021).

[30] S. Thapa, R. Paudel, M. D. Blanchet, P. T. Gemperline, and R. B. Comes, J. Mater. Res. **36**, 26 (2021).

[31] Z. Yang, C. Ko, and S. Ramanathan, Annu. Rev. Mater. Res. **41**, 337 (2011).

[32] M. Golalikhani *et al.*, Nat. Commun. **9**, 2206 (2018).

[33] E. J. Moon, B. A. Gray, M. Kareev, J. Liu, S. G. Altendorf, F. Strigari, L. H. Tjeng, J. W. Freeland, and J. Chakhalian, New J. Phys. **13**, 073037 (2011).

[34] A. V. Boris *et al.*, Science **332**, 937 (2011).

[35] R. Eguchi, A. Chainani, M. Taguchi, M. Matsunami, Y. Ishida, K. Horiba, Y. Senba, H. Ohashi, and S. Shin, Phys. Rev. B **79**, 115122 (2009).

[36] J. Son, P. Moetakef, J. M. LeBeau, D. Ouellette, L. Balents, S. J. Allen, and S. Stemmer, Appl. Phys. Lett. **96**, 062114 (2010).

[37] R. Scherwitzl, S. Gariglio, M. Gabay, P. Zubko, M. Gibert, and J.-M. Triscone, Phys. Rev. Lett. **106**, 246403 (2011).

[38] A. X. Gray *et al.*, Phys. Rev. B **84**, 075104 (2011).

[39] P. D. C. King *et al.*, Nat. Nanotechnol. **9**, 443 (2014).

[40] J. C. Woicik *et al.*, Phys. Rev. B **64**, 125115 (2001).

[41] S.-H. Yang, B. S. Mun, A. W. Kay, S.-K. Kim, J. B. Kortright, J. H. Underwood, Z. Hussain, and C. S. Fadley, Surf. Sci. **461**, L557 (2000).

[42] S.-H. Yang *et al.*, Phys. Rev. B **84**, 184410 (2011).

[43] S.-H. Yang *et al.*, J. Phys.: Condens. Matter **18**, L259 (2006).

[44] A. J. Grutter *et al.*, Phys. Rev. Lett. **111**, 087202 (2013).

[45] C. L. Flint, H. Jang, J.-S. Lee, A. T. N'Diaye, P. Shafer, E. Arenholz, and Y. Suzuki, Phys. Rev. Mater. **1**, 024404 (2017).

[46] C. L. Flint, A. Vailionis, H. Zhou, H. Jang, J.-S. Lee, and Y. Suzuki, Phys. Rev. B **96**, 144438 (2017).

[47] V. R. Galakhov *et al.*, Phys. Rev. B **65**, 113102 (2002).

[48] L. Qiao and X. Bi, Europhys. Lett. **93**, 57002 (2011).

[49] B. R. K. Nanda, S. Satpathy, and M. S. Springborg, Phys. Rev. Lett. **98**, 216804 (2007).

[50] I. C. Tung *et al.*, Phys. Rev. Mater. **1**, 053404 (2017).

[51] S. Nemsak *et al.*, Nat. Commun. **5**, 5441 (2014).

[52] O. Karslıoğlu *et al.*, Faraday Discuss. **180**, 35 (2015).

[53] A. Ohtomo and H. Y. Hwang, Nature **427**, 423 (2004).

[54] J. A. Bert, B. Kalisky, C. Bell, M. Kim, Y. Hikita, H. Y. Hwang, and K. A. Moler, Nat. Phys. **7**, 767 (2011).

[55] A. Brinkman *et al.*, Nat. Mater. **6**, 493 (2007).

[56] G. Berner *et al.*, Phys. Rev. Lett. **110**, 247601 (2013).

[57] P. Moetakef, J. Y. Zhang, A. Kozhanov, B. Jalan, R. Seshadri, S. J. Allen, and S. Stemmer, Appl. Phys. Lett. **98**, 112110 (2011).

[58] C. Jackson, P. Moetakef, S. J. Allen, and S. Stemmer, Appl. Phys. Lett. **100**, 232106 (2012).

[59] P. Moetakef *et al.*, Appl. Phys. Lett. **99**, 232116 (2011).

[60] S. Nemšák *et al.*, Appl. Phys. Lett. **107**, 231602 (2015).

[61] R. B. Comes *et al.*, Adv. Mater. Interfaces **3**, 1500779 (2016).

[62] R. B. Comes, S. R. Spurgeon, D. M. Kepaptsoglou, M. H. Engelhard, D. E. Perea, T. C. Kaspar, Q. M. Ramasse, P. V. Sushko, and S. A. Chambers, Chem. Mater. **29**, 1147 (2017).

[63] J. P. Perdew, A. Ruzsinszky, G. I. Csonka, O. A. Vydrov, G. E. Scuseria, L. A. Constantin, X. L. Zhou, and K. Burke, Phys. Rev. Lett. **100**, 136406 (2008).

[64] G. Kresse and J. Hafner, Phys. Rev. B **49**, 14251 (1994).

[65] F. Kronast *et al.*, Appl. Phys. Lett. **93**, 243116 (2008).

[66] A. X. Gray *et al.*, Appl. Phys. Lett. **97**, 062503 (2010).

[67] D. Kutnyakhov *et al.*, Ultramicroscopy **130**, 63 (2013).

[68] C. Tusche, A. Krasyuk, and J. Kirschner, Ultramicroscopy **159**, 520 (2015).

[69] G. Schönhense *et al.*, Ultramicroscopy **183**, 19 (2017).